Incoherent digital holographic adaptive optics

Myung K. Kim

Department of Physics, University of South Florida, Tampa, Florida 33620, USA (mkkim@usf.edu)

Received 15 August 2012; accepted 5 October 2012;
posted 15 October 2012 (Doc. ID 174381); published 6 November 2012

An adaptive optical system based on incoherent digital holography is described. Theoretical and experimental studies show that wavefront sensing and compensation can be achieved by numerical processing of digital holograms of incoherent objects and a guide star, thereby dispensing with the hardware components of conventional adaptive optics systems, such as lenslet arrays and deformable mirrors. The incoherent digital holographic adaptive optics (IDHAO) process is seen to be robust and effective under various ranges of parameters, such as aberration type and strength. Furthermore, low and noisy image signals can be extracted by IDHAO to yield high-quality images with good contrast and resolution, both for point-like and continuous extended objects, illuminated with common incoherent light. Potential applications in astronomical and other imaging systems appear plausible.

OCIS codes: 110.1080, 090.1995, 350.1260.

1. Introduction

Light from distant stars and galaxies travels through the near perfect vacuum of space for millions of years, carrying information about the distant parts of the universe, until the last fraction of a second when it plunges through the Earth's atmosphere before reaching our eyes or telescopes on the ground. Atmospheric turbulence causes degradation or aberration of images, such that increasing the aperture of a telescope does not lead to improvement of resolution. Placing the telescope in space above the atmosphere, or at least at as high an altitude as possible on top of mountains, alleviates the problem, but at considerable cost and constraint. The concept of adaptive optics (AO), put forward at least several decades ago [1,2], is based on sensing the wavefront and adjusting the optical system in real time to compensate for any distortion. The development of wavefront sensors and compensators with sufficient levels of performance were crucial to implementation of the AO in large telescope systems that began in the 1990s [3]. Remarkable astronomical images have been obtained using ground-based telescopes with AO compensation of atmospheric turbulence, whose quality can surpass even space-based telescopes under favorable conditions [4]. The principle of AO is also applied to other imaging systems, most notably in ophthalmic imaging [5] as well as in laser beam forming and remote sensing [6].

In a typical AO system, a guide star of sufficient brightness is used for measuring the aberration. A common method of wavefront sensing is the Shack–Hartmann sensor, consisting of a lenslet array and a CCD camera underneath it [7]. Distortions of the wavefront lead to shifts of lenslet focal spots, proportional to the local slope of the wavefront. The information is used to compute the necessary displacement of a deformable mirror or other spatial light modulator (SLM). The wavefront sensing, wavefront modulation, and control subsystems form a closed loop to reach a configuration that minimizes the aberration in the image of the full field. Specifications of the AO system are governed by the key parameters of atmospheric turbulence [8]. The Fried parameter is the effective spatial scale of the turbulent eddies, such that it, rather than the telescope aperture, limits the image resolution. The isoplanatic angle is the maximum angular distance between the guide star and the object under observation, which is limited by the distribution of turbulent

1559-128X/13/01A117-14$15.00/0

layers over a range of altitudes. The Greenwood frequency represents the inverse time scale of the turbulence, and therefore dictates the response time of the AO feedback system. Thus, the number of sensor subapertures limits the spatial bandwidth of measurable aberration, while the number and types of actuators in the modulator limit the accuracy and bandwidth of corrections. The speed and accuracy of computation and optomechanical feedback are critical aspects of such an AO system.

We have recently introduced AO principles based on the ability of digital holography (DH) to measure and manipulate optical phase profiles [9]. They replace the wavefront sensor and corrector hardware components with numerical processing by DH [10,11] for wavefront measurement and compensation. The principle of aberration compensation is a well-known characteristic of holography, as demonstrated in the early years of conventional holography [12]. Phase conjugation by nonlinear optics is a dynamic holography process and has been an active area of research and development for applications in AO [13]. More generally speaking, these processes are based on the decoding of an encoded image using its correlation with the key, such as in the Vander Lugt matched filter [14]. In context of AO, the true image is encoded by the aberration, and the aberration key is extracted using the guide star information. DH is particularly versatile and flexible in extracting and manipulating the optical phase profiles, as demonstrated in digital holographic microscopy [15–17]. Compensation of low-order aberrations, including tilt, spherical aberration, and astigmatism, have been demonstrated either by double exposure of the field with and without the specimen, or by assuming a portion of the object field to be flat [18]. Automatic compensation of higher-order terms of the Zernike polynomials has been demonstrated, and a concept of numerical parametric lens has been introduced which can shift, magnify, and compensate for aberrations [19].

Almost all objects of telescopic observations, such as stars and planets, are incoherent sources. A number of techniques have been put forward for holography of incoherent sources since the early years of conventional holography, including the grating achromatic interferometer [20], the triangular interferometer [21], and conoscopic holography [22]. Experimental demonstrations of most of these techniques, however, have been limited to reconstruction of not more than a few point sources. The main difficulty is that although it is possible to generate self-interference of elementary objects, such as point sources, often in the form of Fresnel zone patterns, the interference patterns are incoherent with respect to each of the other point sources. As soon as the number of point sources increases beyond a few, or for objects of extended surfaces, the intensity of interference patterns adds incoherently, rapidly washing out the fringes. On the other hand, in DH, together with the phase shifting technique [23], it is possible to extract the complex amplitude from the interference pattern of each point source. The complex amplitudes then add coherently among all the point sources.

DH can be carried out using incoherent sources in the same manner as using coherent sources, provided that the object and reference arms are maintained at equal path lengths within the margin of the coherence length [24]. But in such a system, the observable depth is limited to the coherence length. Conventional or analog holography of objects larger or deeper than coherence length using an incoherent source presents a particular challenge, as mentioned earlier. On the other hand, a DH adaptation of the triangular interferometer and conoscopic holography, for example, has been shown to overcome the limitations of the analog versions [25,26]. The optical scanning holography is a unique approach to incoherent holography, where a three-dimensional (3D) Fresnel zone pattern is scanned over the object volume [27]. A significant new development is the Fresnel incoherent correlation holography (FINCH), where two copies of the object wave are superposed with an extra phase curvature introduced on one of them, so that every point source on the object produces the Fresnel zone interference pattern [28]. The complex field amplitude is extracted by quadrature shifting of the relative phase between the two copies. FINCH has been demonstrated to be capable of generating color holograms of objects illuminated with arc lamps or holograms of fluorescence [29,30].

In a recent paper [31], we have introduced a new method of AO to measure and compensate aberrations based on incoherent digital holography (IDH) with a modified FINCH interferometer. As with the coherent holographic AO system, the hologram of a guide star contains sufficient information to compensate the effect of an aberration on the full-field hologram. Reconstruction from an uncompensated full-field hologram yields distorted images comparable to direct nonholographic images formed through the same aberrating medium, while the compensated holographic images have much of the aberrations removed. In this paper, we provide full descriptions of the theoretical simulation and experimental studies of the method—incoherent digital holographic adaptive optics (IDHAO)—that we have carried out. The IDHAO process is seen to be robust and efficient under various ranges of parameters, such as aberration types and strength. Furthermore, low-image signals buried under noise can be extracted by IDHAO to yield high-quality images with good contrast and resolution, both for point-like sources and continuous extended objects illuminated with common incoherent light sources. We begin with a theoretical description of image reconstruction in incoherent DH and aberration compensation and AO in IDH in Section 2, followed by simulation studies in Section 3 that visualize theoretical predictions. A series of experiments described in Section 4 clearly confirm expected characteristics and capabilities of the

IDHAO system. Theoretical and experimental results are summarized and discussed in Section 5, particularly in view of potential astronomical and other imaging applications. We conclude in Section 6.

2. Theory

Theoretical description of IDHAO is developed by considering propagation of spherical waves from object source points through a variation of a FINCH interferometer, followed by integration of the interference intensities over the source points. A complex hologram is obtained by invoking a phase-shifting procedure, leading to an expression of the holographic image as a convolution of object intensity with a complex point spread function (PSF). Even in the presence an of aberrating layer, under a specific condition, one obtains a holographic image as a convolution but with distorted PSF. A straightforward procedure is described to compensate for the aberration by combining holograms of the full field and a guide star.

A. IDH of Basic Configuration

Consider the essential configuration of IDH, Fig. 1, based on a variation of the FINCH interferometer, where the pixel-sharing SLM is replaced with a modified Michelson interferometer. The beam-splitter (BS) produces two copies of the spherical wave emanating from each point source of an object, and the two mirrors (M_A and M_B), equidistant from BS, add different curvatures to the spherical waves. Two copies of the same optical field are always coherent with each other. Therefore, when they are superposed at the camera plane, they produce Fresnel zone-like interference patterns. Specifically, consider a point source of strength $I_o = |E_o|^2$ on $\Sigma_o(x_o, y_o)$-plane a distance z_o from the curved mirrors. First, consider IDH imaging without the aberrator Ψ in place. The field reflecting from M_A and arriving at the camera plane $\Sigma_c(x_c, y_c)$ a distance z_c from the mirror is, under Fresnel or paraxial approximation [10]:

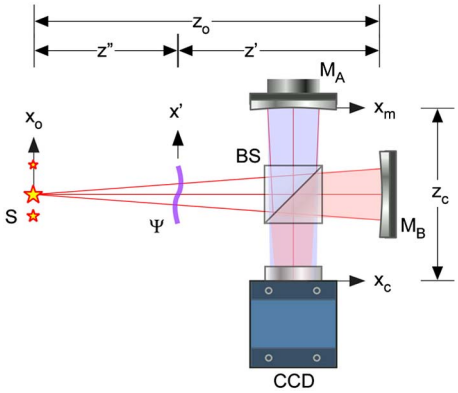

Fig. 1. (Color online) Basic configuration of IDH. S, source point; Ψ, phase aberrator; BS, beam splitter; M_A (M_B), curved mirror with focal length f_A (f_B).

$$E_A(x_c) = \int dx_m E_o Q_{z_o}(x_m - x_o) Q_{-f_A}(x_m) Q_{z_c}(x_c - x_m) = E_o Q_{z_o - f_A}(x_o) Q_{z_A + z_c}(x_c - x_A), \quad (1)$$

where Q represents the quadratic phase function

$$Q_z(x) \equiv \exp\left[\frac{ik}{2z}x^2\right], \quad (2)$$

and $(x_A, y_A; z_A)$ is the image position of the source point through the curved mirror:

$$x_A = -\frac{f_A}{z_o - f_A}x_o; \qquad z_A = -\frac{f_A}{z_o - f_A}z_o. \quad (3)$$

For compactness of expressions, we ignore overall propagation factors of the form $\exp(ikz)$ as well as constant factors, and abbreviate all (x, y)-terms with (x) only. The wavelength is $\lambda = 2\pi/k$. In these calculations, it is useful to note a basic property:

$$Q_{z_1}(x - x_1) Q_{z_2}(x - x_2) = Q_{z_1 + z_2}(x_1 - x_2) Q_{z_{12}}(x - x_{12}), \quad (4)$$

with

$$z_{12} = \frac{z_1 z_2}{z_1 + z_2}; \qquad x_{12} = \frac{z_2 x_1 + z_1 x_2}{z_1 + z_2}. \quad (5)$$

The other mirror, with focal length, f_B generates another output field $E_B(x_c)$ with similar definitions of x_B and z_B. The two components superpose and interfere to produce the Fresnel zone-like intensity pattern recorded by the camera. One of the cross-terms is

$$G_0(x_c; x_o) = E_A E_B^* = I_o(x_o) Q_{z_{AB}}(x_c - \alpha x_o), \quad (6)$$

so that the intensity at the camera is

$$g(x_c; x_o) = |E_A + E_B|^2 = 2I_o(x_o)\left[1 + \cos\frac{k(x_c - \alpha x_o)^2}{2z_{AB}}\right], \quad (7)$$

where

$$\alpha = -\frac{z_c}{z_o}$$
$$z_{AB} = -\frac{(z_A + z_c)(z_B + z_c)}{z_A - z_B}. \quad (8)$$

The point-source interference intensity $g(x_c; x_o)$ has the familiar concentric ring pattern of radially increasing frequency.

For an extended object illuminated by incoherent light, the source points are incoherent with each other. Therefore, the total intensity is the sum or integral of the point-source interference intensities $g(x_c; x_o)$ contributed by all the source points:

$$h(x_c) = \int \mathrm{d}x_o g(x_c; x_o), \tag{9}$$

which, as soon as a significant number of source points add up, quickly washes out the fringe structures. On the other hand, the phase-shifting process can be applied to extract the integral of the complex cross term. One of the mirrors, M_A, is piezo-mounted so that a global phase φ can be applied. Then the interference intensity is

$$h_\varphi(x_c) = \int \mathrm{d}x_o g_\varphi(x_c; x_o) = \int \mathrm{d}x_o |E_A e^{i\varphi} + E_B|^2, \tag{10}$$

and a four-step phase-shift process yields

$$\begin{aligned} H_0(x_c) &= (1/4)\{[h_0 - h_\pi] - i[h_{\pi/2} - h_{3\pi/2}]\} \\ &= \int \mathrm{d}x_o G_0(x_c; x_o) \\ &= \int \mathrm{d}x_o I_o(x_o) Q_{z_{AB}}(x_c - \alpha x_o) \\ &= I'_o \odot Q_{z_{AB}}(x_c), \end{aligned} \tag{11}$$

where

$$I'_o(x_c) = I_o\left(\frac{x_c}{\alpha}\right) \tag{12}$$

is the scaled object intensity pattern and the symbol $\odot$ represents the convolution. The subscript 0 in G_0 and H_0 signifies the absence of aberration. That is, one obtains a complex hologram as a convolution of the object intensity I'_o with a complex PSF $Q_{z_{AB}}$ [32]. For holographic reconstruction, the complex hologram $H_0(x_c)$ is back propagated by the distance $-z_{AB}$:

$$I'_o(x_c) = H_0 \odot Q_{-z_{AB}}(x_c). \tag{13}$$

B. IDH with Aberration

Now, consider IDH imaging in the presence of the phase aberrator $\Psi(x')$ at the $\Sigma'(x', y')$ plane. The field component A arriving at the output plane $\Sigma_c(x_c, y_c)$ is now

$$\begin{aligned} E_A(x_c) &= \int \mathrm{d}x' \int \mathrm{d}x_m E_o Q_{z''}(x' - x_o) \Psi(x') \\ &\quad \times Q_{z'}(x_m - x') Q_{-f_A}(x_m) Q_{z_c}(x_c - x_m) \\ &= E_o Q_{z_o - f_A}(x_o) Q_{z_A + z_c}(x_c - x_A) \Phi_A(x_c - \alpha_A x_o), \end{aligned} \tag{14}$$

where

$$\Phi_A(x) = [\Psi \odot Q_{\zeta_A}](\beta_A x) = \int \mathrm{d}x' \Psi(x') Q_{\zeta_A}(x' - \beta_A x), \tag{15}$$

and

$$\begin{aligned} \alpha_A &= -\frac{z'}{z''}\frac{z_A + z_c}{z_A} + \alpha, \\ \beta_A &= \frac{z''}{z'' + z'}\frac{z_A}{z_A + z_c}, \\ \zeta_A &= \frac{z''}{z'' + z'}\left[z' + \frac{z''}{z'' + z'}\frac{z_A z_c}{z_A + z_c}\right]. \end{aligned} \tag{16}$$

Combining with a similar expression for E_B, we obtain the complex hologram of a single source point

$$\begin{aligned} G_\Psi(x_c; x_o) &= E_A E_B^* \\ &= I_o(x_o) Q_{z_o - f_A}(x_o) Q^*_{z_o - f_B}(x_o) Q_{z_A + z_c}(x_c - x_A) \\ &\quad \times Q^*_{z_B + z_c}(x_c - x_B) \Phi_A(x_c - \alpha_A x_o) \Phi^*_B(x_c - \alpha_B x_o) \\ &= I_o(x_o) Q_{z_{AB}}(x_c - \alpha x_o) \Phi_A(x_c - \alpha_A x_o) \\ &\quad \times \Phi^*_B(x_c - \alpha_B x_o), \end{aligned} \tag{17}$$

and for an extended object

$$\begin{aligned} H_\Psi(x_c) &= \int \mathrm{d}x_o G_\Psi(x_c; x_o) \\ &= \int \mathrm{d}x_o I_o(x_o) Q_{z_{AB}}(x_c - \alpha x_o) \\ &\quad \times \Phi_A(x_c - \alpha_A x_o) \Phi^*_B(x_c - \alpha_B x_o). \end{aligned} \tag{18}$$

C. IDHAO by Compensation of Aberration

The last integral is turned into a convolution if we set $z' = 0$, as described below, so that $\alpha_A = \alpha_B = \alpha$. Then

$$G_\Psi(x_c; x_o) = I_o(x_o)[Q_{z_{AB}} \Phi_A \Phi^*_B](x_c - \alpha x_o), \tag{19}$$

and

$$H_\Psi(x_c) = I'_o \odot [Q_{z_{AB}} \Phi_A \Phi^*_B](x_c). \tag{20}$$

Aberration compensation for AO proceeds as follows. A hologram of a guide star of unit magnitude at the center of the field is acquired to yield

$$G_\Psi(x_c) \equiv G_\Psi(x_c; 0) = [Q_{z_{AB}} \Phi_A \Phi^*_B](x_c). \tag{21}$$

The full-field complex hologram $H_\Psi(x_c)$ is then

$$H_\Psi(x_c) = I'_o \odot G_\Psi(x_c). \tag{22}$$

Attempt to reconstruct by numerical propagation $Q_{-z_{AB}} = G_0^*$ corresponds to

$$I_\Psi \equiv H_\Psi \odot G_0^* = H_\Psi \otimes G_0 = I'_o \odot [G_\Psi \otimes G_0], \tag{23}$$

which, in general, does not yield an accurate reproduction of the object I'_o. The symbol $\otimes$ stands for correlation. On the other hand, use of the guide star hologram leads to

$$\hat{I}_\Psi \equiv H_\Psi \otimes G_\Psi = I'_o \odot [G_\Psi \otimes G_\Psi] \approx I'_o \odot \delta = I'_o. \quad (24)$$

That is, as long as the auto-correlation of the guide star hologram is sharp enough, the result is an accurate reproduction of the object I'_o. Note that in the absence of the aberration the delta function is exact, $G_0 \otimes G_0 = \delta$. Equivalently, the hologram aberration can be compensated by subtracting the phase error of G_Ψ from H_Ψ in the Fourier domain. That is

$$\hat{I}_\Psi = \hat{H}_\Psi \odot G_0^*, \quad (25)$$

where

$$\hat{H}_\Psi = H_\Psi \otimes (G_\Psi \otimes G_0). \quad (26)$$

The latter method involves an additional correlation operation, but it has the flexibility of being able to recenter the guide star hologram G_0 to avoid lateral shift of the final full-field reconstructed image.

For comparison, one can also calculate the direct image formed when one of the mirrors M_B focuses the image on the camera plane, while the other mirror is blocked, so that

$$\begin{aligned} I_B(x_c) &= \int dx_o |E_B(x_c; x_o)|^2 \\ &= \int dx_o I_o(x_o) |\Phi_B(x_c - \alpha x_o)|^2. \end{aligned} \quad (27)$$

When focused, we have $z_B + z_c = 0$ so that $\beta_B \to \infty$ and $\zeta_B \to \infty$. But closer examination of the exponent in $Q_{\zeta_B}(x' - \beta_B x)$ shows that

$$|\Phi'_B(x_c)|^2 = |\tilde{\Psi}(x_c)|^2, \quad (28)$$

where $\tilde{\Psi}$ is the Fourier transform of Ψ:

$$\tilde{\Psi}(x_c) = \int dx' \Psi(x') \exp\left[-ik \frac{x_c}{z_c} x'\right], \quad (29)$$

so that

$$I_B(x_c) = [I'_o \odot |\tilde{\Psi}|^2](x_c). \quad (30)$$

As expected, the PSF is absolute square of the Fourier transform of the aperture.

3. Simulation

We have carried out a series of simulation studies to characterize the predictions of the theory. The IDHAO is implemented experimentally using the optical configuration depicted in Fig. 2, and the simulation assumes a similar configuration. The objective lens L_o of focal length f_o forms an intermediate image in front of the interferometer. The phase aberrator Ψ is placed close to the lens L_o. The relay lens L_a of focal length f_a is used to image the phase aberrator Ψ onto the mirrors, achieving the requirement

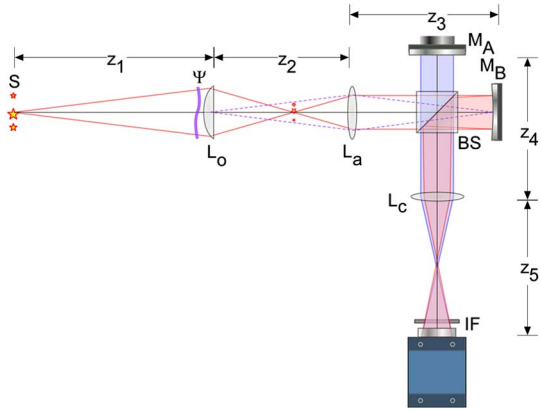

Fig. 2. (Color online) Optical configuration used in simulation and experiments. M_A, piezo-mounted plane mirror; M_B, curved mirror with focal length f_B; L's, lenses; IF, interference filter.

of $z' = 0$. The imaging lens L_c is used in combination with L_o to adjust the magnification and resolution of the system [33,34]. The interference filter (IF) helps improve the interference contrast. One of the mirrors, M_A, is planar and piezo-mounted for phase-shifting process, while the other mirror, M_B, is curved with focal length f_B.

A. IDH

First, a basic IDH process, without any aberration, is illustrated in Fig. 3 where we use the pattern of the Big Dipper as our object field I_o [Fig. 3(a)]. Each frame is 256 pixels and 10 mm across. The assumed optical configuration is such that the light from each point source arrives on the mirrors as a plane wave. The mirror M_B has focal length $f_B = 3000$ mm, the imaging lens L_c is absent, and the camera is at $z_c = z_4 + z_5 = 1000$ mm from the mirrors, so that the holographic image distance is $z_i = 2000$ mm. The wavelength is set $\lambda = 633$ nm. One of the four phase-shifted interference pattern, h_φ, on the camera plane is shown in Fig. 3(b), which we refer to as the raw interferograms. A combination of four such interferograms yields the complex hologram H_0, whose amplitude and phase profiles are shown in Figs. 3(c) and 3(d), respectively. In most of the illustrations in this paper, complex images are shown with a pair of amplitude and phase images. The amplitude images are rendered with the Matlab definition of "jet" color map, while for the phase images, the blue-white-red color map corresponds to the range $[-\pi, \pi]$. Numerical propagation of the complex hologram to an appropriate distance results in the reconstructed image I'_o in Figs. 3(e) and 3(f).

B. IDHAO

The adaptive optics or aberration compensation process by IDHAO is illustrated in Fig. 4, where we start with the same input image I_o in Fig. 4(a). The assumed phase aberration profile Ψ, Fig. 4(b), consists of two Zernike polynomial terms, $\Psi = a_\Psi(Z_3^{+1} + Z_5^{-1})$ with $a_\Psi = -0.5$. The raw interferogram g_φ for the guide star and h_φ for full-field illumination are

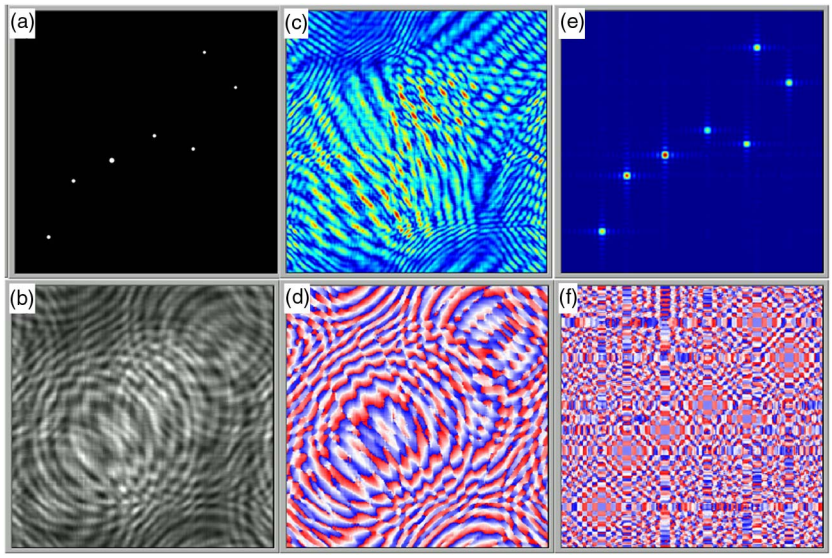

Fig. 3. (Color online) Simulation of IDH process: (a) Object field, I_o; (b) one of raw interferograms h_φ on the camera plane; (c) amplitude; (d) phase of the complex hologram H_0; (e) amplitude; and (f) phase of reconstructed image I'_o.

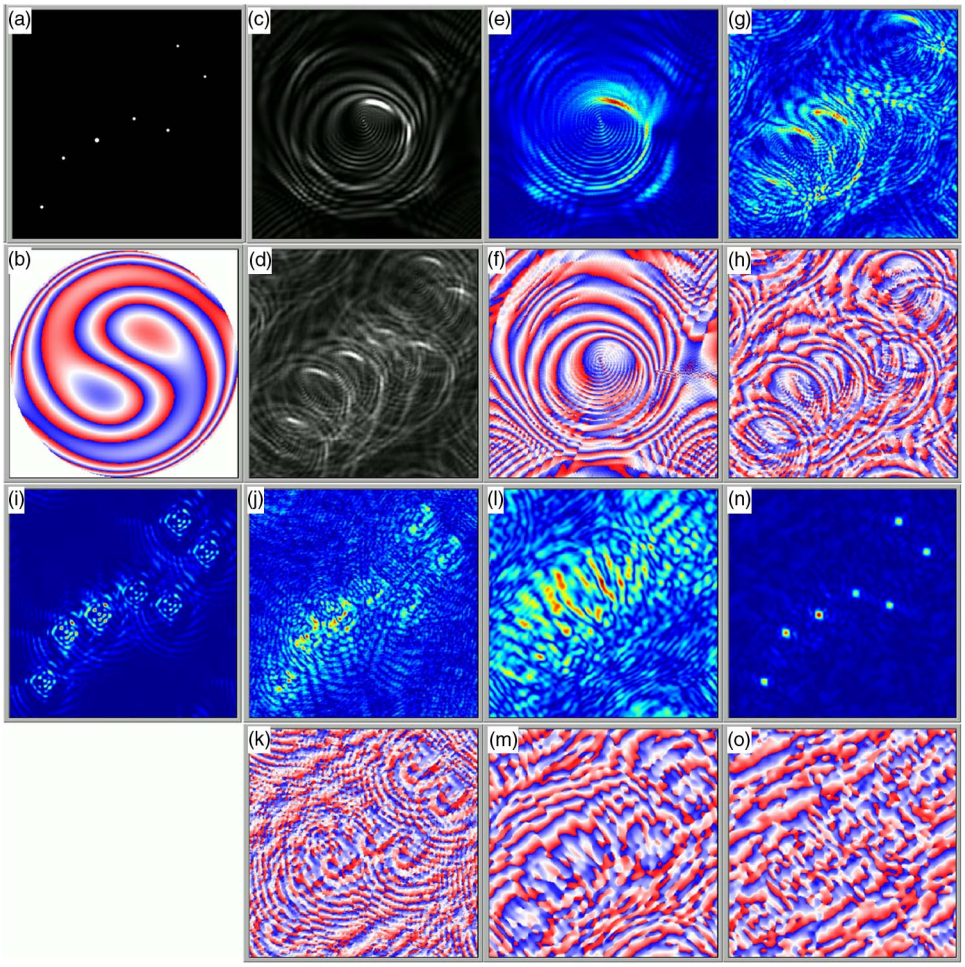

Fig. 4. (Color online) Simulation of the AO process by IDH: (a) the object field I_o, (b) the assumed phase aberration $\Psi = a_\Psi(Z_3^{+1} + Z_5^{-1})$ with $a_\Psi = -0.5$, (c) one of the guide star interferograms g_φ, (d) and (e) the guide star complex hologram G_Ψ, (f) one of the full-field interferograms h_φ, (g) and (h) the full-field complex hologram H_Ψ, (i) direct image I_B without holographic process, (j) and (k) IDH image I_Ψ without aberration compensation, (l) and (m) complex hologram $\hat{H}_\Psi$ with aberration compensation (n) and (o) IDH image $\hat{I}_\Psi$ with aberration compensation. (Note the somewhat irregular arrangement of subpanel labels.)

shown in Figs. 4(c) and 4(f), respectively. A set of four quadrature phase-shifted interferograms combine to produce the complex holograms G_Ψ in Figs. 4(d) and 4(e) for the guide star and H_Ψ in Figs. 4(g) and 4(h) for the full field. Figure 4(i) is the expected direct image I_B through the aberrator without any holographic process, while Figs. 4(j) and 4(k) show the reconstruction I_Ψ from the hologram H_Ψ. Both I_B and I_Ψ show serious degradation due to the aberration. The compensated hologram $\hat{H}_\Psi$ is shown in Figs. 4(l) and 4(m). Note that the vortex-like structures in Fig. 4(h) have been replaced by more concentric ones in Fig. 4(m). Aberration-compensated image $\hat{I}_\Psi$ is obtained in Figs. 4(n) and 4(o) by numerical propagation from the compensated hologram $\hat{H}_\Psi$, or equivalently by correlation of H_Ψ and G_Ψ. The compensated image $\hat{I}_\Psi$ is seen to have removed much of the distortions seen in the direct image I_B or the uncompensated holographic image I_Ψ, resulting in well-focused image of the point sources of I_o.

C. Parametric Behavior of IDHAO

Behavior of IDHAO is simulated as several different parameters are varied, including the resolution, aberration strength, and aberration type. IDHAO is seen to be effective under a wide range of these parameters, as well as under increasing noise added to the phase profile. Aberration compensation is also expected to be equally effective for extended continuous objects as well as point-source objects.

As shown in Fig. 5(a), the resolution of the IDHAO-reconstructed images is found to be consistent with the expected behavior of $\delta x \propto \lambda f_B/a$, where $a =$ 10 mm is the frame size and the mirror M_A is planar, while the focal length of M_B is varied over a range. In Fig. 5(b), an aberration $\Psi = a_\Psi(Z_3^{+1} + Z_5^{-1})$ with $a_\Psi = -0.5$ is assumed. Evidently, the resolution of the reconstructed image is not significantly affected by the aberration when compensated by IDHAO, and behaves in an otherwise similar manner as in Fig. 5(a). The image resolution is also expected to depend on the arrangement of the imaging lens L_c and the camera with respect to the overlap of the reflections from the two mirrors M_A and M_B, though we did not include the imaging lens in our simulation [33,34].

The behavior of the IDHAO with increasing strength of aberration is illustrated in Fig. 6. The aberration is varied for (a) $a_\Psi = -0.1$, (b) $a_\Psi = -0.2$, (c) $a_\Psi = -0.5$, and (d) $a_\Psi = -1.0$ of the same type $\Psi = a_\Psi(Z_3^{+1} + Z_5^{-1})$ as above. Other parameters are as in Fig. 4. The aberration phase profiles are displayed on the left of each row. Then, I_Ψ is the uncompensated holographic image and $\hat{I}_\Psi$ is the holographic image compensated by IDHAO, while the direct image I_B is also shown for comparison. That is, I_Ψ or I_B are the "before" images, while $\hat{I}_\Psi$ is the "after" image. It is seen that the compensated image maintains reasonable quality for even a high level of aberration, whereas both the uncompensated and direct images deteriorate quite rapidly. For the strongest aberration in Fig. 6(d), the aberration completely obliterates the uncompensated image I_Ψ and the direct image I_B, though the latter develops a numerical artifact that makes the obliteration less obvious. However, the compensated image $\hat{I}_\Psi$ still maintains good resolution and contrast. On the other hand, note that while the compensated image $\hat{I}_\Psi$ maintains relatively sharp central peaks, the peak height does decrease and broader halo develops around each peak as the aberration increases.

The IDHAO process is equally effective for various types of aberrations, as shown in Fig. 7. In particular, the effectiveness of IDHAO is not contingent upon the symmetry of the aberration profile. Note that the uncompensated images I_Ψ and I_B show similar patterns of distortion for each type of aberration, and the compensation removes most of the distortions in $\hat{I}_\Psi$.

Next, in Fig. 8, a gray scale photographic image is used as the model object, most other parameters being the same as before. Because of the large

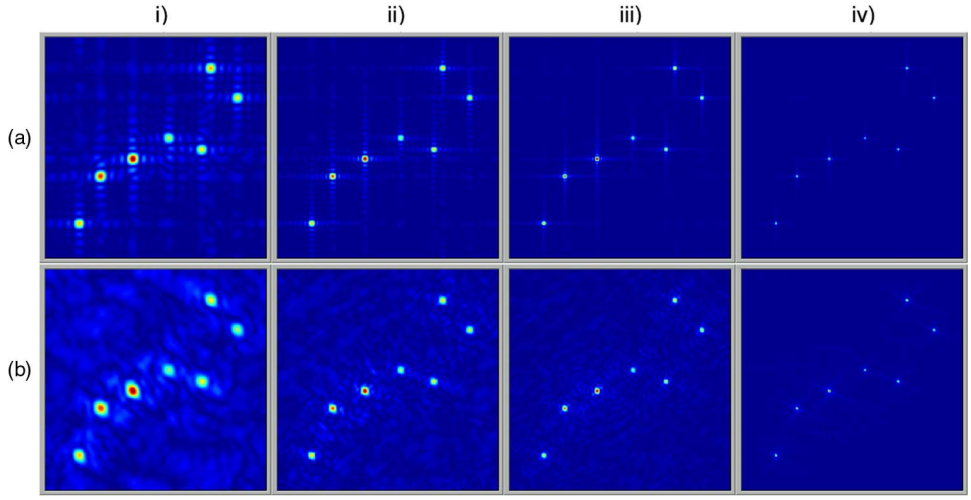

Fig. 5. (Color online) Resolution of reconstructed images $\hat{I}_\Psi$ versus focal length: (a) without aberration $a_\Psi = 0.0$ and (b) with aberration $a_\Psi = -0.5$. The focal length of M_B is varied as $f_B =$ (i) 5000, (ii) 3000, (iii) 2000, and (iv) 1000 mm, while $z_i = f_B - z_c$.

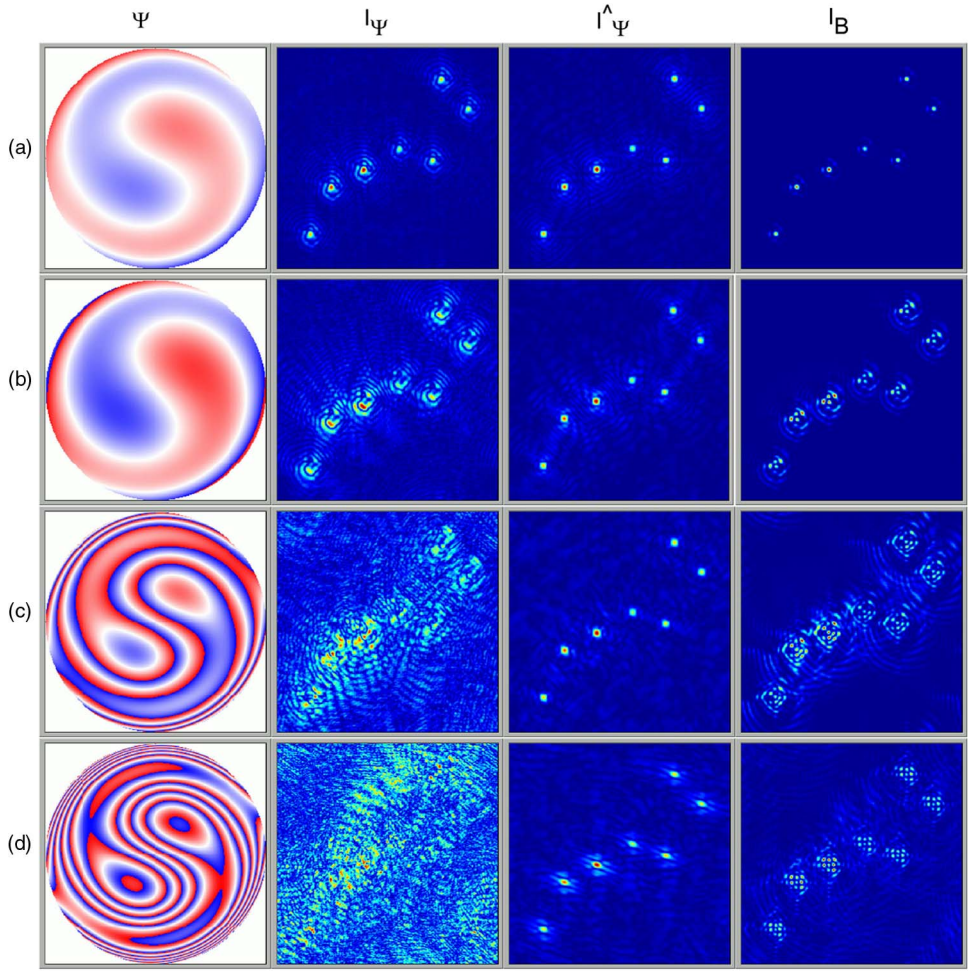

Fig. 6. (Color online) IDHAO versus strength of aberration. In each row the phase aberration Ψ, the uncompensated image I_Ψ, the compensated image $\hat{I}_\Psi$, and the direct image I_B are shown. Strength of the aberration $\Psi = a_\Psi(Z_3^{+1} + Z_5^{-1})$ is varied as (a) $a_\Psi = -0.1$, (b) $a_\Psi = -0.2$, (c) $a_\Psi = -0.5$, and (d) $a_\Psi = -1.0$.

number of nonzero object pixels, the computation is substantially longer compared to the preceding simulations, where the object consisted of seven illuminated pixels—the IDHAO process needs to be calculated for each source point before integrating over all pixels. However, the IDHAO process is seen to behave as expected and is able to remove much of the distortion and mostly recover the resolution loss due to the assumed phase aberration.

Lastly, we look at the behavior of IDHAO in the presence of noise. In Fig. 9, the noise is simulated by adding random phase noise on the complex holograms G_Ψ and H_Ψ. A phase of a_Φ times a random number in the range [0,1] is added to each pixel in the holograms, with $a_\Phi = 5$ for rows (a) and (c) or $a_\Phi = 10$ for rows (b) and (d). The first two rows (a) and (b) assume no aberration, $a_\Psi = 0$, while the lower two rows (c) and (d) assume $a_\Psi = 0.2$, in $\Psi = a_\Psi(Z_3^{+1} + Z_5^{-1})$. The phase noise in each case is significant enough to almost obscure the underlying Fresnel ring patterns, though not completely. Reconstructed images I_Ψ without compensation suffers, and, especially when a small amount of aberration is present, the noise almost completely obliterates the signal. On the other hand, the compensated images $\hat{I}_\Psi$ degrade only mildly even when both phase noise and aberration are present. This behavior is remarkable but also reasonable, in view of the fact that $\hat{I}_\Psi$ is the correlation of H_Ψ with G_Ψ, meaning that any noise or aberration in H_Ψ that has low correlation with G_Ψ does not have significant contribution to the final image $\hat{I}_\Psi$.

Note that this simulates noise in the detection system, not in the optical field itself. Noise in the optical field is accounted for as aberration if it is present at a plane conjugate to the interferometer mirrors. Noise, or aberration, away from the conjugate plane is not compensated by the present scheme of IDHAO, unless one sets up a multiconjugate configuration, which may be possible borrowing some of the techniques available in conventional AO systems [3].

4. Experiment

We have carried out a series of experiments to confirm the results of theoretical and simulation studies, and to observe general behavior of the IDHAO process. First, to demonstrate the basic IDH with focusing property, the optical configuration of Fig. 2

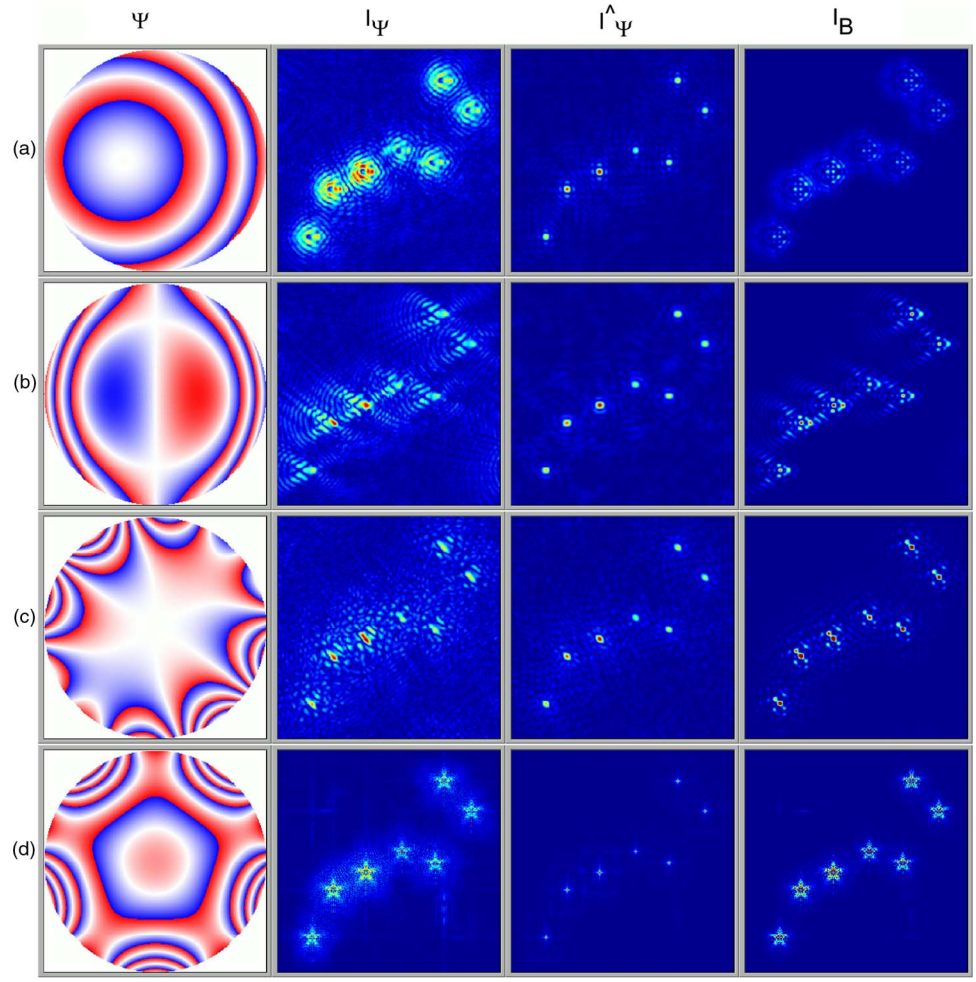

Fig. 7. (Color online) IDHAO versus various types of aberration: (a) $\Psi = (-0.5) \times Z_1^{+1} + (-0.5) \times Z_2^0$, (b) $\Psi = (-0.5) \times Z_1^{+1} + (-0.5) \times Z_3^{+1}$, (c) $\Psi = (-0.5) \times Z_3^{+3} + (-0.5) \times Z_5^{-5}$, and (d) $\Psi = (-0.7) \times Z_2^0 + (-0.5) \times Z_5^{-5}$.

is set up using a group of three red LED's at $z_1 =$ 650 mm and another red LED closer at $z_1' =$ 440 mm. All three lenses are of focal length $f_o = f_a = f_c = 100$ mm, while the curved mirror has $f_B = 600$ mm. Various distances are set at $z_2 = 220$ mm, $z_3 = 200$ mm, $z_4 = 200$ mm, and $z_5 =$ 140 mm, ±5 mm. The Pixelfly CCD camera has a 6.3 mm × 4.8 mm sensor area with 640 × 480 pixels, which projects to an approximately 60 mm × 45 mm field of view at the object plane at z_1 from L_o. The plane mirror M_A is piezo-mounted and driven with the sawtooth output of a digital function generator and four phase-shift interferograms are acquired at 20 fps. Hologram acquisition, reconstruction, and aberration compensation are carried out by LabVIEW-based programs. The entire cycle takes a few seconds, including file write/read and without any attempt to optimize the speed.

A. IDH

One of the raw holograms h_φ of the four-LED object field is shown in Fig. 10(a) and the corresponding complex hologram H_0 in Fig. 10(b). One may note the slightly higher fringe frequency of the lower left

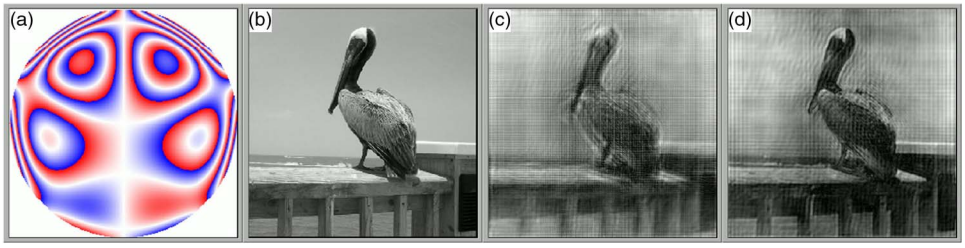

Fig. 8. (Color online) IDHAO of extended gray-scale object: (a) the assumed phase aberration $\Psi = (0.5) \times (Z_5^{+3} + Z_4^{-2})$, (b) object I_o, (c) uncompensated image I_Ψ, and (d) compensated image $\hat{I}_\Psi$.

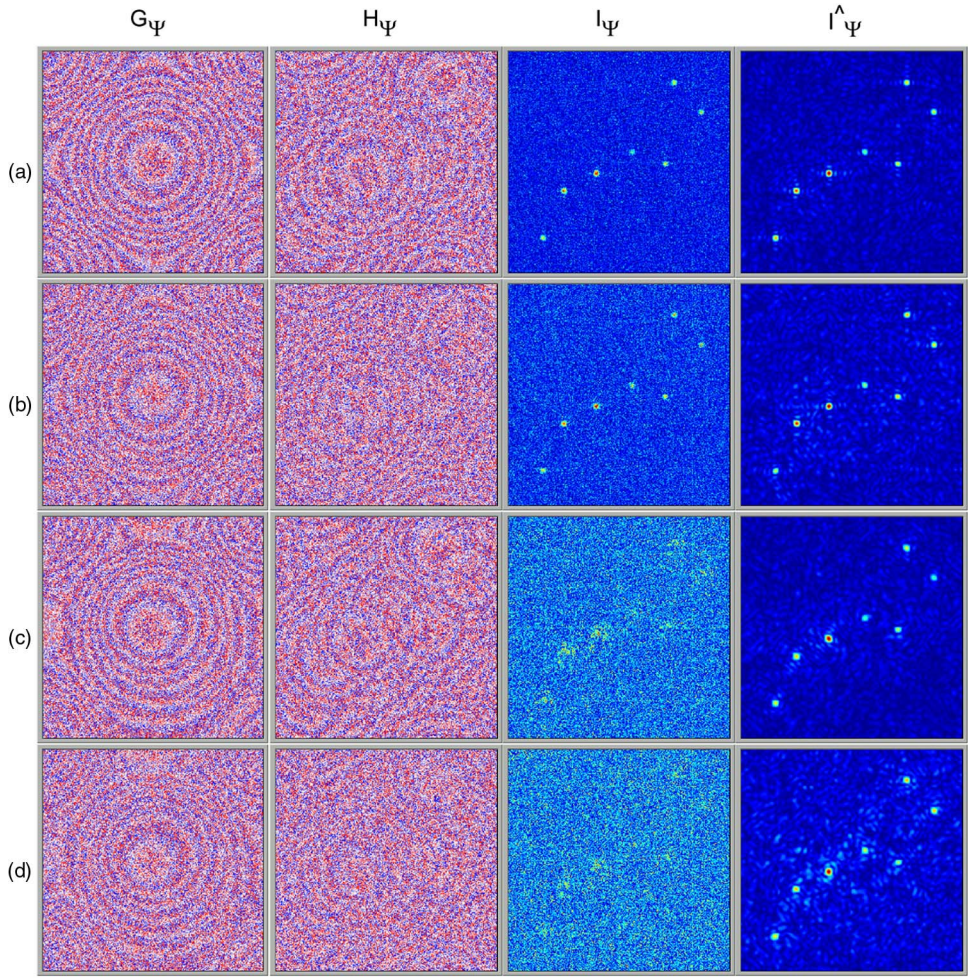

Fig. 9. (Color online) Effect of noisy hologram on IDHAO: (a) $a_\Psi = 0$, $a_\Phi = 5$; (b) $a_\Psi = 0$, $a_\Phi = 10$; (c) $a_\Psi = 0.2$, $a_\Phi = 5$; (d) $a_\Psi = 0.2$, $a_\Phi = 10$. In each row the phase of G_Ψ and H_Ψ and the amplitude of I_Ψ and I' are shown.

LED, compared to the other three LEDs, due to its closer distance to the objective lens. Numerical propagation of the hologram focuses the LEDs at two separate distances, (c) at $z_i = 22000$ mm and (d) at $z_i = 14870$ mm, whose values are consistent with the effective image distances projected to the object space. The image distances can be calculated by using Eq. (8) and geometrical optics consideration, and the approximate 10:1 lateral magnification corresponds to 100:1 longitudinal magnification.

B. IDHAO

Phase aberrators are fabricated by coating an optically clear plastic piece with acrylic paint to produce irregular surface profiles of varying degrees. An aberrator is placed just behind the objective lens

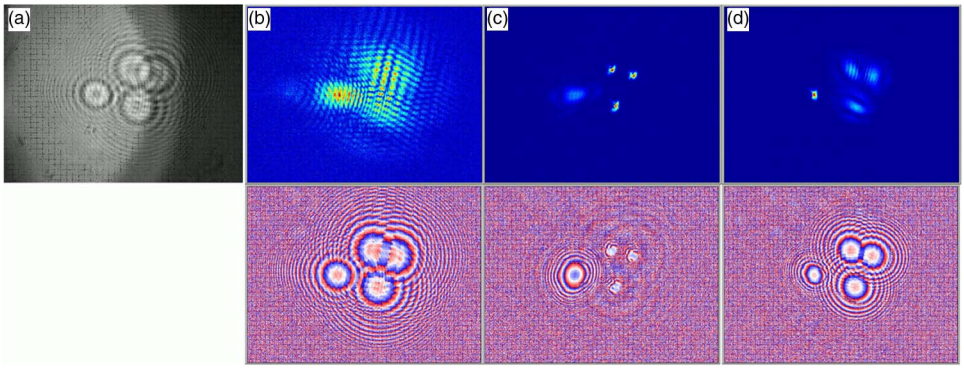

Fig. 10. (Color online) IDH without aberration: (a) one of the raw holograms h_φ; (b) complex hologram H_0; (c) reconstructed image at $z_i = 22,000$ mm;, corresponding to $z_1 = 650$ mm; (d) reconstructed image at $z'_i = 14,870$ mm; corresponding to $z'_1 = 440$ mm.

L_o, and the resulting IDH images are shown in the upper row of Fig. 11. The concentric rings of Figs. 10(a) and 10(b) are now replaced with severely distorted patterns in Fig. 11(a) and 11(b). An attempt to numerically focus the images from H_Ψ yields Fig. 11(c) and 11(d) at the two expected image distances. Now a guide star hologram G_Ψ is acquired by aperturing the object field to leave only one of the LEDs on, in this case one belonging to the three-LED group at $z_1 = 650$ mm, as shown in Fig. 11(e). Aberration compensation using the guide star hologram, as described in theory and simulation, then results in the corrected hologram $\hat{H}_\Psi$ in Fig. 11(f) and the corrected images $\hat{I}_\Psi$ in Fig. 11(g) and 11(h). Note, as in simulation of Fig. 4, that the distorted fringes in Fig. 11(b) are replaced with more concentric ones in Fig. 11(f). Note also that the guide star at z_1 is effective in compensating the images at both z_1 and z_1'. Another test, not presented, of using a guide star at z_1' was equally effective in compensating the images at the two distances. That is, a guide star can be placed at any distance relative to the object volume. This is a unique property of IDHAO, which may not be available in other existing AO techniques.

C. Noise

Next, the LED brightness is reduced to various levels to observe effects of noise and low signals on the IDH and IDHAO images. In Fig. 12, all four LEDs are placed at $z_1 = 650$ mm, which constitutes the object field. One of them, the leftmost one, is also used as the guide star. No deliberate aberrator is in place. In each row of Fig. 12, the first image, column (i), is the reconstructed image I_Ψ without compensation, while columns (ii)–(iv) are the compensated images $\hat{I}_\Psi$ with increasing brightness of the guide star. The rows (a)–(c) represent the object field with decreasing brightness. In all cases, the IDHAO process is seen to be capable of reducing the noise and increasing the contrast. Also, it is significant to note that the contrast enhancement increases as the guide star brightness. The effect is especially marked for the weakest signal in (c), where the uncompensated image is almost buried in the background, but the brighter guide star brings out the signal with high contrast, while maintaining good resolution.

D. Extended Objects

In addition to the point-like sources of LEDs, extended objects of finite surfaces are also used to test the IDHAO process. In the top row of Fig. 13, a miniature halogen lamp illuminates a resolution target from behind through a piece of frosted glass, while in the bottom row, a knight chess piece is illuminated with the halogen lamp in front. The objects are at $z_1' = 450$ mm. In both cases an IF, centered at 600 nm and of linewidth 10 nm, is placed in front of the camera to improve the interference contrast, although we have not noticed significant difference in resulting images. In each case, a raw interferogram h_φ and the complex hologram H_Ψ are shown. Note that for these extended objects, the raw interferograms only have barely recognizable interference contrast. No deliberate phase aberrator is present.

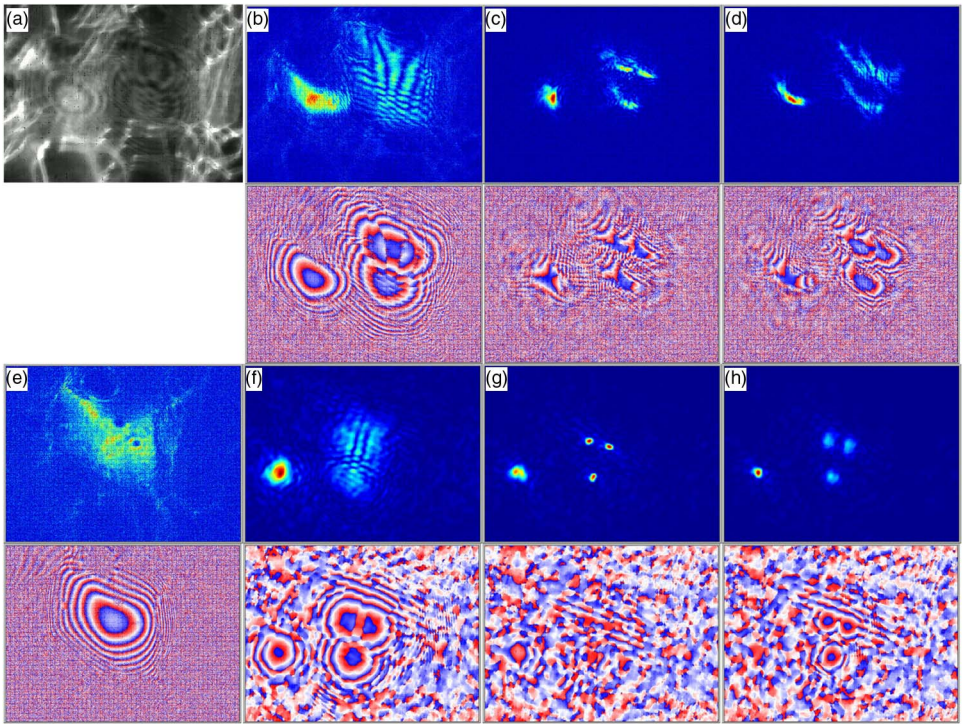

Fig. 11. (Color online) IDHAO with a phase aberrator placed just behind the objective lens: (a) one of the raw holograms h_φ; (b) complex hologram H_Ψ, reconstructed images I_Ψ; (c) at z_i; (d) at z_i'; (e) guide star hologram G_Ψ of an LED at z_1; (f) corrected hologram $\hat{H}_\Psi$, corrected images $\hat{I}_\Psi$; (g) at z_i; and (h) at z_i'.

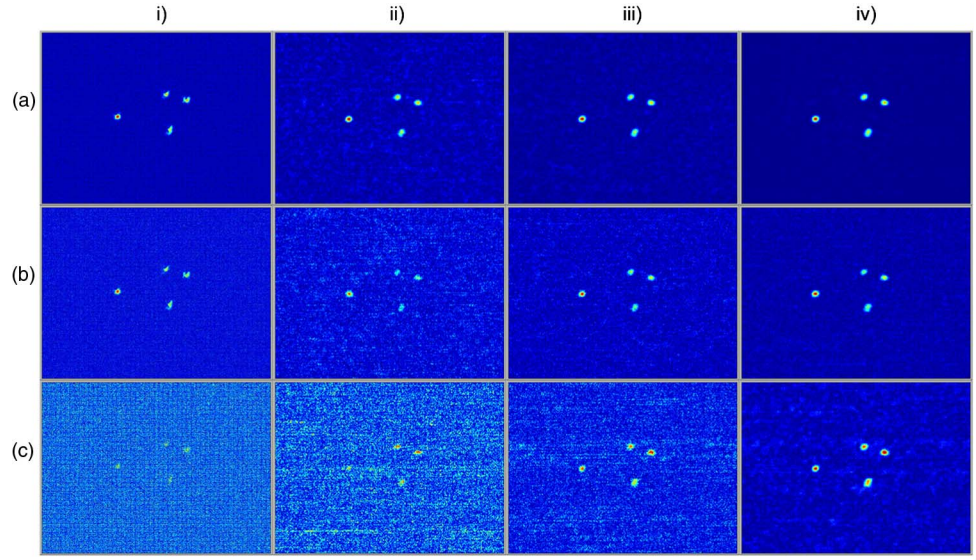

Fig. 12. (Color online) IDHAO versus noise: (a)–(c) varying brightness of the object field, consisting of all four LEDs; (i) IDH image I_Ψ without AO; (ii)–(iv) IDHAO images $\hat{I}_\Psi$, with varying brightness of the guide star.

An LED placed next to the objects at $z_1' = 450$ mm serves as the guide star.

In Fig. 14, an experiment similar to that of Fig. 12 is carried out by varying the brightness of the halogen lamp and the guide star LED. Again, it is seen that the IDHAO process is quite effective in extracting and strengthening the image signals buried in background noise.

Finally, Fig. 15 shows that the IDHAO process is effective for a 3D object volume, as we found for LED objects in the experiment of Fig. 11. In this experiment, an LED at $z_1 = 650$ mm is turned on in addition to the knight piece at $z_1' = 450$ mm—the guide star LED is still at the same distance as the knight. In the corrected images of the bottom row, as well as the uncorrected images of the top row, the objects separately come into clear focus at the appropriate distances.

5. Discussion

The IDHAO is described to be an effective and robust means of compensating optical aberrations in incoherent optical imaging systems. Theoretical framework based on propagation of spherical waves from source points followed by integration of intensity over the object points correctly predicts the possibility of aberration compensation. General behavior of the theoretical model of IDHAO is illustrated by simulation studies. They show robust aberration compensation under various ranges of parameters, including aberration type and strength, as well as in presence of significant noise. Finally, experimental studies corroborate these predictions extremely well. The IDHAO process is seen to be effective for both point-like sources and extended objects. In particular, a brighter guide star is seen to be very effective in bringing out weak signals buried under noise

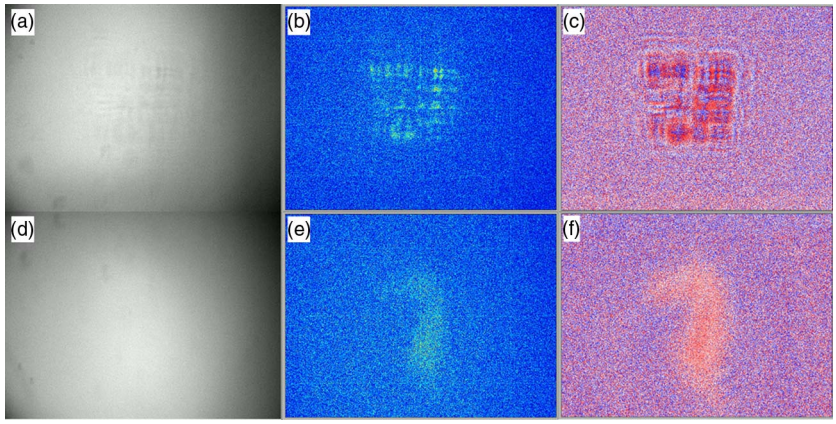

Fig. 13. (Color online) IDH of extended objects, a resolution target (top) and a knight chess piece (bottom), illuminated with a miniature halogen lamp. In each case, a raw hologram h_φ and the amplitude and phase of the complex hologram H_Ψ are shown.

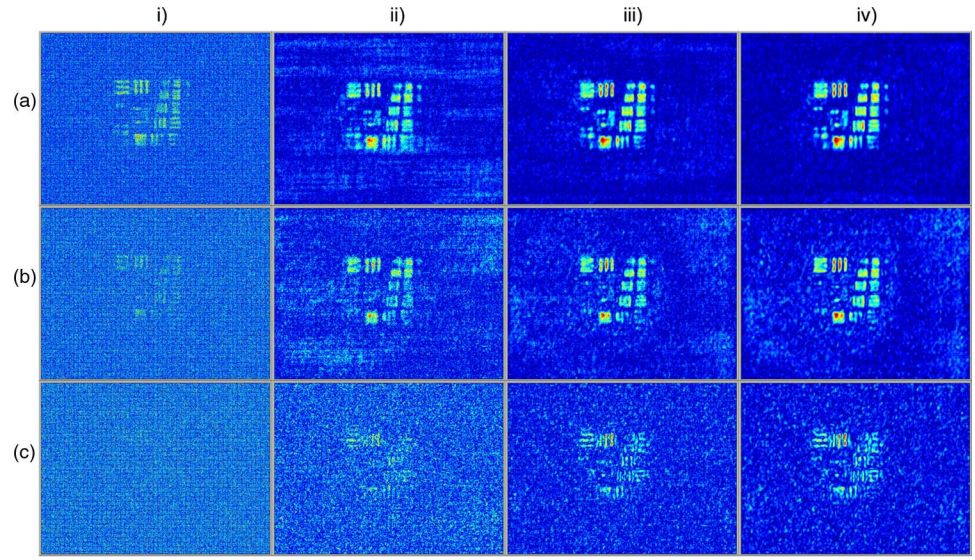

Fig. 14. (Color online) IDHAO versus noise: (a)–(c) varying brightness of the resolution target, (i) IDH image I_Ψ without AO; (ii)–(iv) IDHAO images $\hat{I}_\Psi$, with varying brightness of the guide star.

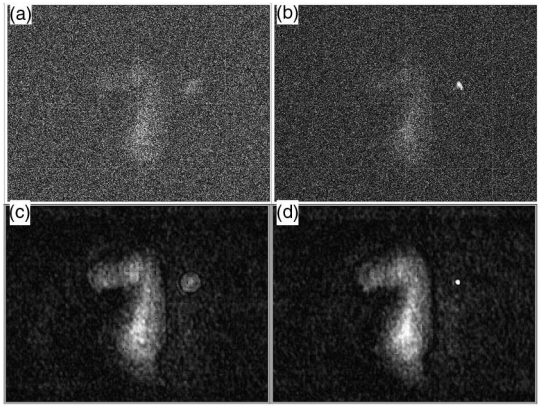

Fig. 15. 3D focusing of IDHAO of extended object: (a) uncorrected image I_Ψ reconstructed at $z_i' = 17,500$ mm, corresponding to $z_1' = 450$ mm; (b) reconstructed image at $z_i = 22,000$ mm, corresponding to $z_1 = 650$ mm; (c) and (d) corresponding images $\hat{I}_\Psi$ with compensation.

through the fact that the IDHAO signal is proportional to the auto-correlation of the complex guide star hologram.

The main results of these theoretical, simulation, and experimental studies can be summarized as follows.

- Theoretical framework is obtained that accurately describes the IDH in the presence of aberration, as well as its compensation by IDHAO.
- Simulation studies based on the theoretical framework closely predict experimental observations.
- Aberration compensation in IDHAO is effective over various ranges of parameters, including resolution, aberration type, aberration strength, and presence of noise.
- The guide star can be placed at any distance relative to the object plane and the aberration compensation by IDHAO applies to the entire 3D object volume.
- Increasing brightness of guide star leads to enhanced contrast of the compensated image, while maintaining good resolution for a noisy input signal.
- All of the basic properties of IDHAO apply to both pointlike and extended continuous objects.

Other than observation and verifications at several representative values, the study of parametric behavior of IDHAO in this work has been mostly qualitative. Our next task is to establish a quantitative comparison of IDHAO with conventional AO systems, considering such factors as resolution, dynamic range, sensitivity, isoplanatic angle, and operating speed. The resolution is mostly determined by the telescopic input image, as long as the interferometer configuration is optimized. The dynamic range and lateral resolution of aberration compensation in IDHAO are, in principle, unlimited. Strong and weak aberrations are handled in exactly the same manner, assuming that the aberration is not so severe that it cannot be described as a phase profile at a plane conjugate to the interferometer plane—but this is the same assumption taken in a conventional system. The lateral resolution of aberration compensation is all of the CCD pixel resolution, which is a very different situation than in a conventional system, where it is limited by the number of actuators in the deformable mirror. The isoplanatic angle for multilayered turbulence is under the same constraint as with conventional AO systems. As with conventional systems, a multiconjugate configuration is feasible, but at significant cost of complexity. The sensitivity or the achievable Strehl ratio using IDHAO, compared to conventional AO, would be first governed by the efficiency of the IDH holographic image formation, which entails formation of the fringes and computation of the holographic images from the acquired fringes. It is also affected, as we have seen above, by the noise suppression aspect of the guide star correlation. The operating speed may depend,

over a large range, on the mode of operation. The IDHAO as described here can be considered an open loop feed forward approach, where the two inputs—the full-field and guide-star holograms—are combined to provide the output. There is no feedback. In that sense, the operating speed is instantaneous, as long as the two holograms are acquired simultaneously, for example by splitting the telescope input beam into two parts with separate interferometers for the full-field and guide-star holograms.

We may also comment on the comparison of the interferometer used in our IDHAO with the FINCH interferometer. In FINCH, a single SLM is used in effect to create a superposition of two lenses. This is done by either using one-half of the pixel count to create each of the two components [28] or by using polarization dependence of the SLM to create the two curvatures for the two polarization components [33]. The IDHAO utilizes the full aperture in a straightforward manner. The presence of the SLM array structure in the beam path in FINCH can cause diffraction sidelobes, an issue that needs to be dealt with. On the other hand, the FINCH configuration is, in principle, mechanically more compact and stable compared to IDHAO.

6. Conclusions

Theoretical, simulation, and experimental studies show that the IDHAO system has many of the desirable properties of conventional AO systems at substantially reduced complexity, and very likely cost, of the optomechanical system. Wavefront sensing and correction by IDHAO have almost the full resolution of the CCD camera. The dynamic range of deformation measurement is essentially unlimited. One can clearly envision potential applications in astronomical and other imaging systems. Work is in progress to study details of key parameters for astronomical imaging, including resolution, sensitivity, and speed, as well as for ophthalmic and other imaging applications.

References

1. H. W. Babcock, "The possibility of compensating astronomical seeing," Publ. Astron. Soc. Pac. **65**, 229–236 (1953).
2. H. W. Babcock, "Adaptive optics revisited," Science **249**, 253–257 (1990).
3. J. W. Hardy, *Adaptive Optics for Astronomical Telescopes* (Oxford University, 1998).
4. R. K. Tyson, *Principles of Adaptive Optics* (CRC Press, 2011).
5. J. Porter, *Adaptive Optics for Vision Science: Principles, Practices, Design, and Applications* (Wiley, 2006).
6. S. Avino, E. Calloni, J. T. Baker, F. Barone, R. DeRosa, L. DiFiore, L. Milano, and S. R. Restaino, "First adaptive optics control of laser beam based on interferometric phase-front detection," Rev. Sci. Instrum. **76**, 083119 (2005).
7. R. K. Tyson, *Introduction to Adaptive Optics* (SPIE, 2000).
8. M. C. Roggemann, B. M. Welsh, and R. Q. Fugate, "Improving the resolution of ground-based telescopes," Rev. Mod. Phys. **69**, 437–506 (1997).
9. C. G. Liu and M. K. Kim, "Digital holographic adaptive optics for ocular imaging: proof of principle," Opt. Lett. **36**, 2710–2712 (2011).
10. M. K. Kim, *Digital Holographic Microscopy: Principles, Techniques, and Applications* (Springer, 2011).
11. M. K. Kim, "Principles and techniques of digital holographic microscopy," SPIE Rev. **1**, 018005 (2010).
12. J. Upatnieks, A. V. Lugt, and E. N. Leith, "Correction of lens aberrations by means of holograms," Appl. Opt. **5**, 589–593 (1966).
13. R. A. Fisher, *Optical Phase Conjugation* (Academic, 1983).
14. A. V. Lugt, "Signal detection by complex spatial filtering," IEEE Trans. Inf. Theory **10**, 139–145 (1964).
15. J. Kuhn, F. Charriere, T. Colomb, E. Cuche, F. Montfort, Y. Emery, P. Marquet, and C. Depeursinge, "Axial subnanometer accuracy in digital holographic microscopy," Meas. Sci. Technol. **19**, 074007 (2008).
16. B. Rappaz, A. Barbul, F. Charriere, J. Kuhn, P. Marquet, R. Korenstein, C. Depeursinge, and P. J. Magistretti, "Erythrocytes analysis with a digital holographic microscope," Proc. SPIE **6631**, 66310H (2007).
17. C. J. Mann, L. F. Yu, C. M. Lo, and M. K. Kim, "High-resolution quantitative phase-contrast microscopy by digital holography," Opt. Express **13**, 8693–8698 (2005).
18. L. Miccio, D. Alfieri, S. Grilli, P. Ferraro, A. Finizio, L. De Petrocellis, and S. D. Nicola, "Direct full compensation of the aberrations in quantitative phase microscopy of thin objects by a single digital hologram," Appl. Phys. Lett. **90**, 041104 (2007).
19. T. Colomb, F. Montfort, J. Kuhn, N. Aspert, E. Cuche, A. Marian, F. Charriere, S. Bourquin, P. Marquet, and C. Depeursinge, "Numerical parametric lens for shifting, magnification, and complete aberration compensation in digital holographic microscopy," J. Opt. Soc. Am. A **23**, 3177–3190 (2006).
20. E. N. Leith and J. Upatniek, "Holography with achromatic-fringe systems," J. Opt. Soc. Am. **57**, 975–980 (1967).
21. G. Cochran, "New method of making Fresnel transforms with incoherent light," J. Opt. Soc. Am. **56**, 1513–1517 (1966).
22. G. Sirat and D. Psaltis, "Conoscopic holography," Opt. Lett. **10**, 4–6 (1985).
23. I. Yamaguchi and T. Zhang, "Phase-shifting digital holography," Opt. Lett. **22**, 1268–1270 (1997).
24. F. Dubois, N. Callens, C. Yourassowsky, M. Hoyos, P. Kurowski, and O. Monnom, "Digital holographic microscopy with reduced spatial coherence for three-dimensional particle flow analysis," Appl. Opt. **45**, 864–871 (2006).
25. S. G. Kim, B. Lee, and E. S. Kim, "Removal of bias and the conjugate image in incoherent on-axis triangular holography and real-time reconstruction of the complex hologram," Appl. Opt. **36**, 4784–4791 (1997).
26. L. M. Mugnier, G. Y. Sirat, and D. Charlot, "Conoscopic holography: two-dimensional numerical reconstructions," Opt. Lett. **18**, 66–68 (1993).
27. T. C. Poon, "Optical scanning holography—a review of recent progress," J. Opt. Soc. Korea **13**, 406–415 (2009).
28. J. Rosen and G. Brooker, "Digital spatially incoherent Fresnel holography," Opt. Lett. **32**, 912–914 (2007).
29. J. Rosen and G. Brooker, "Non-scanning motionless fluorescence three-dimensional holographic microscopy," Nat. Photonics **2**, 190–195 (2008).
30. J. Rosen and G. Brooker, "Fluorescence incoherent color holography," Opt. Express **15**, 2244–2250 (2007).
31. M. K. Kim, "Adaptive optics by incoherent digital holography," Opt. Lett. **37**, 2694–2696 (2012).
32. J. Rosen, N. Siegel, and G. Brooker, "Theoretical and experimental demonstration of resolution beyond the Rayleigh limit by FINCH fluorescence microscopic imaging," Opt. Express **19**, 26249–26268 (2011).
33. G. Brooker, N. Siegel, V. Wang, and J. Rosen, "Optimal resolution in Fresnel incoherent correlation holographic fluorescence microscopy," Opt. Express **19**, 5047–5062 (2011).
34. B. Katz, D. Wulich, and J. Rosen, "Optimal noise suppression in Fresnel incoherent correlation holography (FINCH) configured for maximum imaging resolution," Appl. Opt. **49**, 5757–5763 (2010).